Supporting information

Reversible Fermi Level Tuning of a Sb_2Te_3 Topological Insulator by Structural Deformation

Sang Han Park,[1] Jimin Chae,[1] Kwang Sik Jeong,[1] Tae-Hyeon Kim,[1] Hyejin Choi,[1] Mann-Ho Cho,[*,1] Inwoong Hwang,[2,3] Myung-Ho Bae,[2,4] and Chul Kang[5]

[1] Institute of Physics and Applied Physics, Yonsei University, Seodaemun-gu, Seoul, 120-749, Republic of Korea

[2] Korea Research Institute of Standards and Science, Daejeon 305-340, Republic of Korea

[3] Department of Physics, Chungnam National University, Daejeon 305-764, Republic of Korea

[4] Department of Nanoscience, University of Science and Technology, Daejeon 305-350, Republic of Korea

[5] Advanced Photonics Research Institute, Gwangju Institute of Science and Technology, Gwangju, 500-712, Republic of Korea

1. Crystal structure of the Sb$_2$Te$_3$ film

The crystal structure of Sb$_2$Te$_3$ film was investigated using X-ray diffraction (XRD) and transmission electron microscopy (TEM). Figure S1 shows the results for an XRD 2θ/ω scan graph to investigate crystal structure in the normal direction. The a 30 nm thick Sb$_2$Te$_3$ film on polyimide (PI) substrate and Sb$_2$Te$_3$ film on SiO$_2$/Si substrate were measured to calibrate the position of Sb$_2$Te$_3$ peaks with Si reference peak. The resulting XRD peaks are assigned as (00x) peaks of a Sb$_2$Te$_3$ rhombohedral structure along c-axis, except for the Si (002) substrate peak.[1, 2] Although the most intense peak of the Sb$_2$Te$_3$ rhombohedral structure is the (015) peak, there are no observable peaks in the XRD results. This can be interpreted that Sb$_2$Te$_3$ film has a rhombohedral structure with a highly preferred orientation along the c-axis.
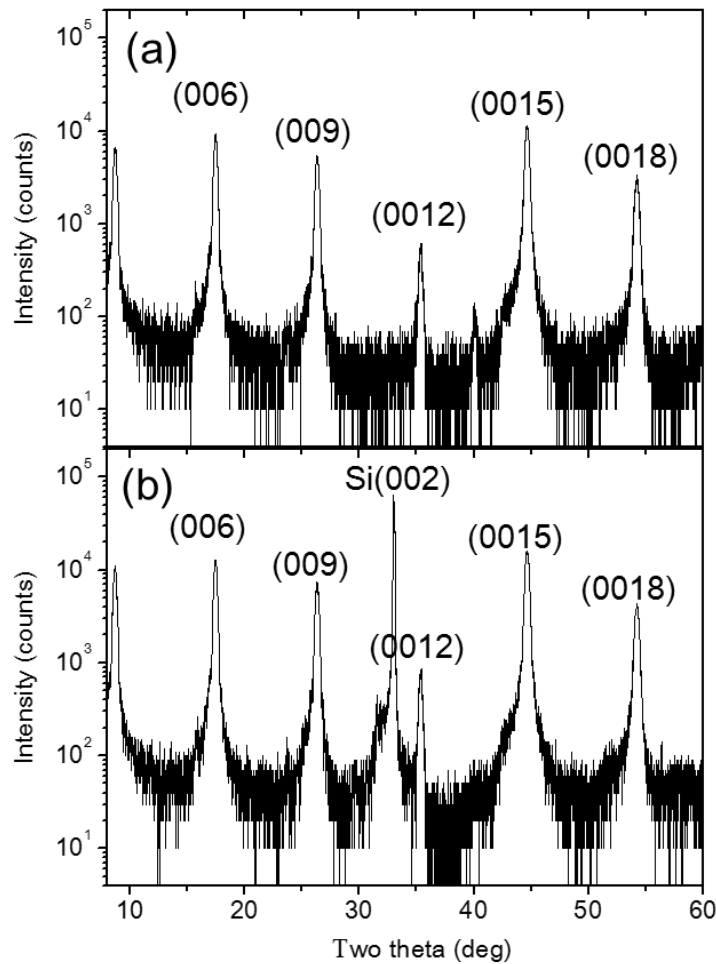

Figure S1. The XRD 2θ/ω measurement result of (a) Sb$_2$Te$_3$ 30nm on PI substrate and (b) Sb$_2$Te$_3$ 30nm on SiO2 100 nm/Si substrate for calibration. The results show that our Sb$_2$Te$_3$ films have the (001) preferred orientation in a direction normal to the substrate with a rhombohedral structure.

Figure S2 (a)~(d) show TEM top view images and reciprocal lattice pattern of a 30 nm thick Sb_2Te_3 film on SiN membrane. The polycrystalline structure was observed with 100~200 nm grain size as shown in Fig. S2 (a). Fig. S2 (b) shows the selected area diffraction (SAD) pattern which is measured with normal direction of SiN membrane, for the region marked in Fig. S2 (a). With same geometry used to Fig. S2 (a and b), Fig. S2 (c and d) show atomic resolution TEM image and its FFT image, respectively. The results show a symmetric diffraction pattern of a Sb_2Te_3 rhombohedral structure matched with the 2.17 Å of lattice distance between the center of the unit cell and the $< 110 >$ planes. To confirm the crystal structure of Sb_2Te_3 on PI substrate, the TEM side view image and converted FFT image of Sb_2Te_3 on PI substrate were measured as shown in Fig. S2 (e) and (f). These can also be interpreted that Sb_2Te_3 film has (001) crystal structure along the normal direction of the film in consistent with the preferred orientation, as shown in in Fig. S1.
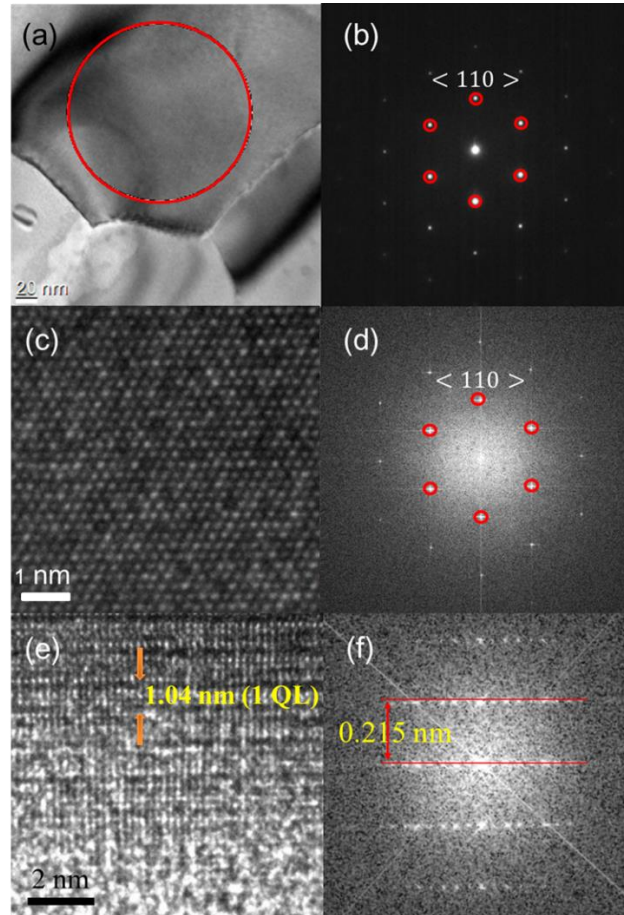

Figure S2. (a) TEM top view image and (b) diffraction pattern of Sb_2Te_3 film on SiN membrane. (c) Atomic resolution TEM image and (d) FFT image for center of (a). (e) TEM side view image and (b) FFT image of Sb_2Te_3 film on PI substrate. The results show that Sb_2Te_3 film has a (001) single crystal structure along the normal direction of the film.

2. Reversibility of resistance control

We propose that mechanical strain using the bending of a poly imide (PI) substrate is reversible and can be used to control the properties of certain types of materials. To support the reversibility of mechanical strain, we performed cycle tests for resistance change. Figure S3 shows the cycle tests for bending and unbending a sample. To mount a sample tightly with micro stage, the strain was switched between 0.3~0.5 %. This result shows that high and low resistance states are constant for more than 20 cycles which indicate that a repeatable R_s change by structural deformation is practicable without defect production or crack formation.
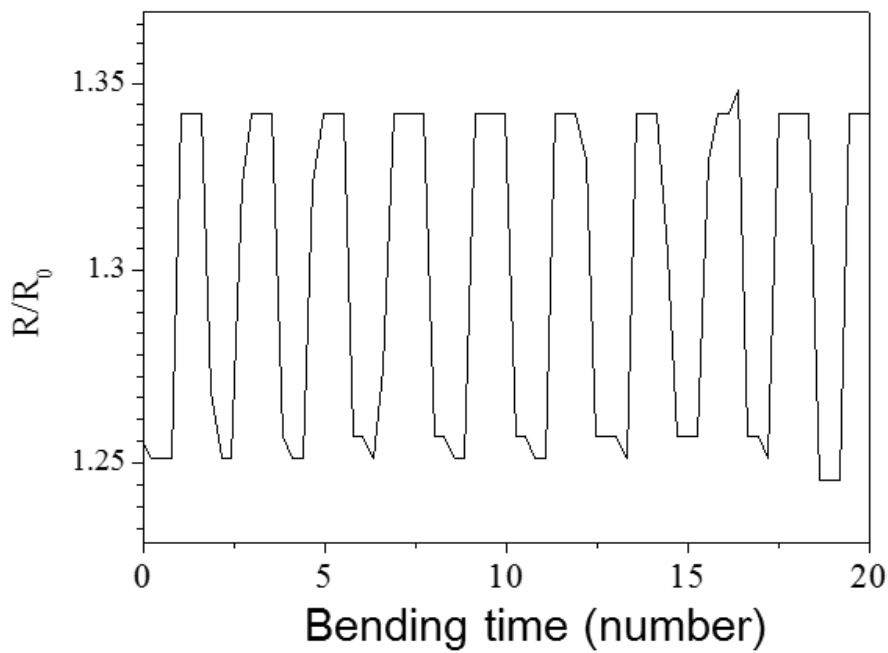
Figure S3. Cycle tests for a small strain from 0.3 % to 0.5 %. The high and low resistance states are constant for more than 20 cycles. This result shows that repeatable R_s change and no defect or crack formation by structural deformation.

One issue of concern in the bending experiment is that fractures or cracks can be produced by structural deformation especially in cases of brittle materials. We checked the optical microscopy image to confirm the damage of Sb_2Te_3 film by excessive strain. As a result, no damage was observed in an optical microscopy image, as shown in Fig. S4.
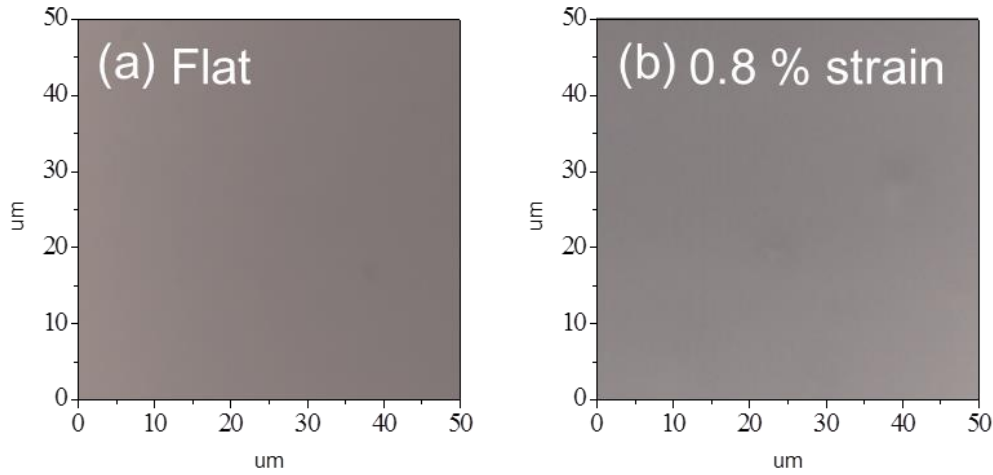
Figure S4. Optical microscopy image of Sb$_2$Te$_3$ films (a) as grown and (b) 0.8 % strained state. No cracks were observed after the bending experiments.

Moreover, Fig. S5 provides information regarding the temperature dependent resistance and magneto resistance measurements after flattening a sample that had previously been bent. The reverse process of strained bending state in Fig. 2, resistance for all temperatures and the change in the MR cusp are decreased for unbent state.   This result indicates that strain can be controlled reversibly using the mechanical bending method.   Also, with the other results mentioned above, our experiments indicate that no cracks or defects were formed.
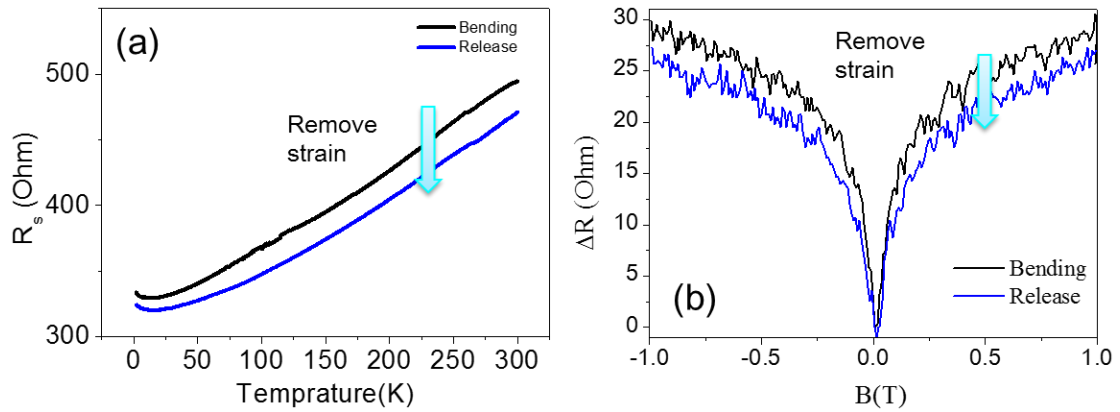

Figure S5. (a) Temperature dependent resistance results show that the resistance decreases for all temperatures after the release of strain. (b) Magneto resistance cusp is decreased for the unbent state. These results come from the increase of carrier density and show that strain can be reversibly controlled using a mechanical bending method.

3. Evidence of a topological surface state

Since the grown Sb_2Te_3 film has a polycrystalline structure, it is difficult to collect angle-resolved photoemission spectroscopy data showing the topological surface state directly. However, there is strong evidence to support the conclusion that the Sb_2Te_3 film has a topological surface state. That is, the WAL effect which is observed for materials with spin momentum locking caused by a topological surface state or a Rashba effect. However, the Rashba effect is observed with asymmetry of the potential induced by surface doping.[3] In addition, for the 2D system which has a coupled surface and bulk channels, Lu and Shen reported that unitary behavior or weak localization (WL) instead of a WAL effect would be expected in the magneto resistance of the bulk band.[4] Therefore, for the case of our Sb_2Te_3 film which has a bulk band gap of 0.3 eV, bulk states occur as the result of a WL effect rather than a WAL effect. Moreover, surface and bulk channels can be decoupled for a thickness of 30 QL, as previously reported, which show the decoupling of surface and bulk channels for the film thicker than 20 QL.[5] For the 30 QL sample, the magneto resistance change of the bulk state is proportional to B^2 up to 9 T, as shown in Fig. S6. Such results are expected for 3D materials in which the surface and bulk states are decoupled.[4] As a result, we can conclude that the WAL effect observed in Fig. S6 should be originated from a metallic surface state where the spin state is locked to the momentum by time-reversal symmetry different from the bulk insulating state.[6,7]
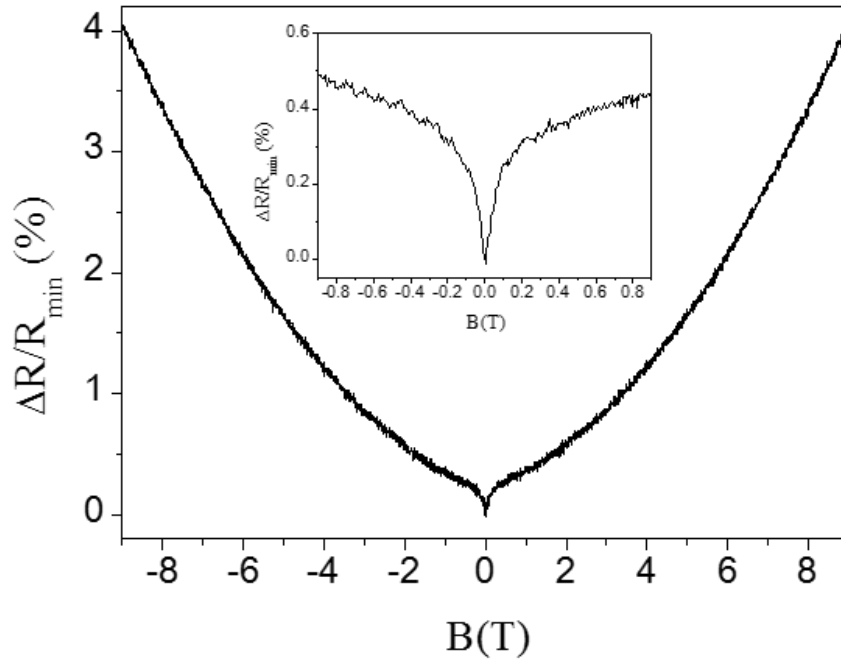

Figure S6. The magneto resistance of flat state Sb_2Te_3 film on PI substrate. The inset shows sharp cusp near zero B-field resulted from the WAL effect of topological surface state. The overall resistance change proportional to B^2 up to 9 T which caused by bulk state.

4. Experimental details

XRS measurements.　The XRS measurements were performed at beamline 1D KIST-PAL, at the Pohang accelerator laboratory (PAL) using a MAR345-image plate detector operating at 3 GeV with a maximum storage current of 300 mA.　The X-ray beam was focused by a toroidal mirror and monochromatized to 10.0094 KeV (1.23868 Å) by a double bounce Si (111) monochromator. The Si(111) monochromator and a Si(111) analyzer crystal were used to provide a high-resolution configuration in reciprocal space.　Though, the scattering patterns were recorded to image plate based on the wavelength value of 1.23868 Å, the XRS spectra shown in the Fig. 1 were integrated after re-calculation of the 2θ values based on the Cu Kα radiation ($\lambda = 1.5414$ Å).

THz time domain spectroscopy.　We used a THz exposure system which delivers optical pulses produced in a 3.5 W Ti:Sapphire regenerative laser amplifier with a center wavelength of 800 nm and a repetition rate of 1 kHz.[8]　The fs laser beam was split into a pump beam and a probe beam by means of a beam splitter.　A pump beam was delivered to a 10×10 mm ZnTe crystal with a thickness of 1 mm to generate THz pulses via optical rectification.　This THz electric filed was mapped out by electro-optic sampling method in another 1 mm thick ZnTe crystal.　The probe beam was delayed using an optical delay line and collinearly focused with the THz beam onto the ZnTe crystal.　In electro-optic sampling, the THz beam induces birefringence in an electro-optic medium.　If the polarized gate pulse traveled through the ZnTe crystal at the same time with THz pulse, the induced birefringence rotated the polarization of the gate pulse.　The magnitude of rotation was proportional to the strength of the THz electric field.　The signal was collected by a combination of a quarter-wave plate, a Wollaston polarizer, and a pair of balanced photodiodes.　The signal current is then sent to a lock-in amplifier (SR830; Stanford Research System, Sunnyvale, CA).　The amplitude spectrum was obtained after Fourier transformation of the THz field, which covered frequencies up to 2.3 THz.　In order to minimize the absorption by water vapor, a region of THz beam path was enclosed and purged with dry air.　A THz low pass filter was used to remove the extra visible source while the experiment was in progress.　In order to avoid thermal effect by THz source, the accumulated pulse energy was kept below 1.0 mW/cm^2.

Measurement of radiated THz field.　The THz emission was detected using reflection geometry at ambient temperature in an air-tight box with a humidity of less than 10 %.　A Ti:Sapphire regenerative laser amplifier with a center wavelength of 800 nm and a repetition rate of 76 MHz was used as the light source.　The fs laser beam was split into a pump beam and a probe beam by a beam splitter.　The pump beam went through a chopper (chopping frequency of 1.7 kHz), while the probe beam was delayed with respect to the pump beam by means of a scanning optical

delay line.   The pump beam was injected into the sample at an angle of 45° and the pump power used to generate THz radiation was 10 mW.   The diameter of the laser spot was approximately 1 mm at the surface of the sample.   The THz radiation from the sample was oriented at an angle of incidence of 45° and focused onto the detector using a pair of parabolic mirrors.   The detection antenna was a Hertzian dipole antenna, with a gap of 5 mm on low temperature-grown GaAs (LT-GaAs) with a detection bandwidth of 0.2–2.5 THz.   The optical power of incident probe beam on the LT-GaAs receiver was 5 mW.   The amplitude spectrum was obtained after Fourier transformation of the THz field, which covered frequencies up to 3.0 THz.

Theoretical calculations. Density functional theory (DFT) calculations were performed with the Vienna ab initio simulation package (VASP) code to verify changes in electronic structure under uni-axial tensile strain.   We used the generalized gradient approximation (GGA) with the Perdew-Burke-Emzerhof for a solid (PBEsol) function.   The initial rhombohedra unit cell structure was geometric optimized with $7{\times}7{\times}7$ k-points, 350 eV and 10^{-5} eV self-consistent field convergence until an energy convergence lower than 0.02 eV/Å was reached.   To describe the strained bulk structure, we deformed the x and y lattice constant in the hexagonal coordination of Sb_2Te_3 based on measured XRS data.   Since XRS can only measure x and y lattices, to determine the lattice constant along the z-axis of this deformed structure, we performed geometry optimization until the stress along z direction was lower than 100 MPa.   In this hexagonal structure, we used $7{\times}7{\times}1$ k-points.   All other conditions were the same as the calculation for the rhombohedra unit cell case.   To simulate the change in surface states under strain, we also calculated six quintuple layers of Sb_2Te_3.   To prevent surface to surface interactions, 30 Å vacuum slab was inserted.   Finally, for geometric optimized deformed structure, a band structure calculation was performed with consideration of spin-orbit coupling effect.   Figure S7 shows the calculated band structure for the flat state and for the 0.8 % strained bending state.   The bulk band structure shifted to higher binding energy while the surface band structure remained at the same point under the tensile strain.
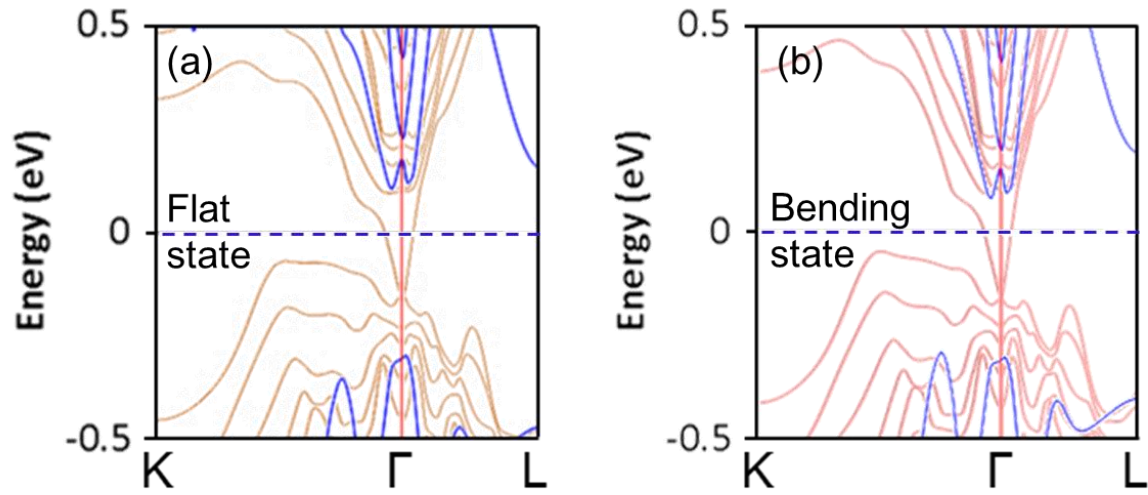
Figure S7. The band structure resulting from density functional theory calculations for (a) the flat state and (b) the 0.8 % strained bending state. The surface states are shown in red and the bulk states in blue. The bulk band structure shifted to higher binding energy while the surface band structure remains at the same point under conditions of tensile strain.

References

(1) Y. Du, M. Huang, T. A. Lograsso, and R. J. McQueeney, X-ray diffuse scattering measurements of chemical short-range order and lattice strains in a highly magnetostrictive $Fe_{0.813}Ga_{0.187}$ alloy in an applied magnetic field. *Phys. Rev. B* **85**, 214437 (2012).

(2) S. A. Semiletov, Kristallografiya. 1, 403 (1956).

(3) P. D. C. King, R. C. Hatch, M. Bianchi, R. Ovsyannikov, C. Lupulescu, G. Landolf, B. Slomski, J. H. Dil, D. Guan, J. L. Mi, E. D. L. Rienks, J. Fink, A. Lindblad, S. Svensson, S. Bao, G. Balakrishnan, B. B. Iversen, J. Osterwalder, W. Eberhardt, F. Baumberger, and Ph. Hofmann, Large Tunable Rashba Spin Splitting of a Two-Dimensional Electron Gas in Bi_2Se_3. *Phys. Rev. Lett.* **107**, 096802 (2011).

(4) H-Z. Lu and S-Q. Shen, Weak localization of bulk channels in topological insulator thin films. *Phys. Rev. B* 84, 125138 (2011).

(5) M. Aitani, T. Hirahara, S. Ichinokura, M. Hanaduka, D. Shin, and S. Hasegawa, In situ magneto transport measurements in ultrathin Bi films: evidence for surface-bulk coherent transport. *Phys. Rev. Lett.* **113**, 206802 (2014).

(6) G. Bergmann, Weak localization in thin films a time-of-flight experiment with conduction electrons, *Phys. Rep.* 107, 1 (1984).

(7) J. Chen, H. J. Qin, F. Yang, J. Liu, T. Guan, F. M. Qu, G. H. Zhang, J. R. Shi, X. C. Xie, C. L. Yang, K. H.Wu, Y. Q. Li, and L. Lu, Gate-voltage control of chemical potential and weak

antilocalization in Bi$_2$Se$_3$, *Phys. Rev. Lett.* 105, 176602 (2010)

(8) J. Park, C. Kim, J. Lee, C. Yim, C.H. Kim, J. Lee, S. Jung, J. Ryu, H.-S. Kang and T. Joo, Generation, transport, and detection of linear accelerator based femtosecond-terahertz pulses. *Rev. Sci. Instrum.* **82**, 013305 (2011).